Available online at www.sciencedirect.com
SCIENCE DIRECT
Catalysis Today 116 (2006) 162–168
CATALYSIS TODAY
www.elsevier.com/locate/cattod

Catalysis science of the solid acidity of model supported tungsten oxide catalysts

Israel E. Wachs *, Taejin Kim, Elizabeth I. Ross

Operando Molecular Spectroscopy and Catalysis Laboratory, Department of Chemical Engineering, 111 Research Drive, Iacocca Hall, Lehigh University, Bethlehem, PA 18015, USA

Available online 5 June 2006

Abstract

A series of supported WO_3 catalysts were synthesized by incipient wetness impregnation of ammonium metatungstate aqueous solutions onto Al_2O_3, TiO_2, Nb_2O_5, and ZrO_2 supports as a function of tungsten oxide loading. The resulting solid acid catalysts were physically characterized with in situ Raman and UV–vis spectroscopy and chemically probed by methanol dehydration to dimethyl ether (CH_3OH-TPSR and steady-state CH_3OH dehydration). The molecular structures of the dehydrated supported tungsten oxide phase were determined to be monotungstate and polytungstate surface WO_x species below monolayer surface coverage (<4.5 W/nm^2), crystalline WO_3 nanoparticles (4.5–9 W/nm^2) and large bulk-like WO_3 crystals (>9 W/nm^2). The electronic structure for the different tungsten oxide species, E_g, was independent of the specific support and decreased monotonically with increasing tungsten oxide domain size (W/nm^2). The solid acid catalytic activity, however, did not correlate with either the molecular or electronic structures because of the dominant contribution by the surface WO_x species to the overall catalytic performance of the supported WO_3 catalysts and its reactivity dependence on the specific support. For supported WO_3/Al_2O_3, the surface WO_x monolayer was more active than the crystalline WO_3 phases and, consequently, the TOF decreased with increasing surface W/nm^2 density. For tungsten oxide supported on Nb_2O_5, TiO_2 and ZrO_2, the surface WO_x monolayer is less active than the crystalline WO_3 phases and, consequently, the TOF increases with surface W/nm^2 density. These reactivity trends reflect the influence of the specific support cation electronegativity on the acid character of the bridging W–O-Support bond.

Keywords: Catalysts; Tungsten oxide; Supported; Alumina; Zirconia; Titania; Niobia; Spectroscopy; Raman; UV–vis; Edge Energy; TPSR; Reaction; Methanol; Oxidative dehydration; Dimethyl ether

1. Introduction

Supported tungsten oxide catalysts consist of tungsten oxide overlayers on high surface area oxide supports (e.g., Al_2O_3, ZrO_2, TiO_2, etc.) [1–30]. The tungsten oxide overlayer can be present as isolated surface monotungstates, polymeric surface polytungstates, crystalline WO_3 particles as well as form compounds with the oxide supports (e.g., $Al_2(WO_4)_3$, $Zr(WO_4)_2$, etc.). The supported tungsten oxide catalysts find numerous applications in the petroleum, chemical, and pollution control industries [31–33]: hydrodesulfurization (HDS) [34] and hydrocarbon cracking (WO_3/Al_2O_3) [35,36], selective catalytic reduction (SCR) of NO_x with NH_3 to form N_2 (V_2O_5–WO_3/TiO_2) [37–39] alkenes isomerization (WO_3/TiO_2) [40,41] alkane isomerization (WO_3/ZrO_2) [15–17] and olefin metathesis (WO_3/SiO_2) [42]. For many of these catalytic applications, the solid acidity of the supported tungsten oxide phase plays a crucial role in their overall catalytic performance. For supported WO_3/Al_2O_3 catalysts, only surface Lewis acid sites are present at low surface coverage and surface Broensted acid sites are also present at intermediate and high surface coverage [5,6,12]. Similar observations have been made for the surface acidity characteristics of supported WO_3/ZrO_2 [16,17,21], WO_3/TiO_2 [10,37,43] and WO_3/Nb_2O_5 [44]. At low surface tungsten oxide coverage (<2 W/nm^2), surface monotungstate species predominate and only Lewis acid character is found to be present. At intermediate tungsten oxide surface coverage (3–4 W/nm^2), surface polytungstate species become predominant and both Broensted acid sites and Lewis acid sites are present. At higher tungsten oxide coverage (>4 W/nm^2),

* Corresponding author. Tel.: +1 610 758 4274; fax: +1 610 758 6555.
E-mail address: iew0@lehigh.edu (I.E. Wachs).

0920-5861/$ – see front matter © 2006 Elsevier B.V. All rights reserved.
doi:10.1016/j.cattod.2006.02.085

crystalline WO_3 nanoparticles (NPs) are present on top of the surface tungstate layer. The molecular level relationships of these different tungsten oxide structures and their surface acidic characteristics are not fully understood at present because of conflicting tungsten oxide structural assignments and the exact surface density where the close packed surface tungsten oxide monolayer forms [4–7,10–15,16–30].

Studies with well defined model supported tungsten oxide catalysts were undertaken in the present study in order to investigate the (1) molecular and electronic structures of the surface monotungstate species, surface polytungstate species and WO_3 NPs, (2) surface tungsten oxide density for close packed monolayer coverage, (3) surface acidity characteristics of the different tungsten oxide structures for methanol dehydration, and (4) the molecular/electronic structure–solid acidity relationship. The term 'model' in the present study refers to preformed supports that are already present in their stable oxide forms (e.g., Al_2O_3, ZrO_2, TiO_2 and Nb_2O_5) and are not present as metastable precursors (e.g., $ZrO(OH)_2$) that will undergo structural changes during the catalysis synthesis steps [8,9]. Comparison of such metastable $ZrO(OH)_2$ supports with preformed model ZrO_2 supports will be the subject of a future communication.

2. Experimental

2.1. Catalyst synthesis

The supported tungsten oxides catalyst were prepared by incipient wet impregnation of aqueous $(NH_4)_{10}W_{12}O_{41}{\cdot}5H_2O$ solutions on the different oxide supports: Al_2O_3 (Harshaw, 178 m^2/g), TiO_2 (Degussa P-25, 51 m^2/g), Nb_2O_5 (CBMM AD1927 HY-340, 66 m^2/g), and ZrO_2 (Degussa, 60 m^2/g). The impregnated samples were initially dried overnight at room temperature, dried at 110 °C for 2 h and then calcined in flowing air for 4 h at 450 °C. The surface tungsten oxide density, W/nm^2, was varied by both increasing the tungsten oxide loading for the 450 °C calcined catalysts as well as sintering the oxide support by calcining at elevated temperatures (700, 800 and 900 °C) for an additional 2 h.

2.2. BET-specific surface area measurement

The BET surface areas of the samples were measured by physical adsorption of N_2 at 77 K (Quantachrome Corp., Model OS-9). The samples were outgassed at 250 °C prior to the N_2 adsorption (Quantachrome Corp., Model QT-3).

2.3. Raman spectroscopy

The molecular structure of the supported tungsten oxide phases was determined with Raman spectroscopy since this technique has the ability to discriminate between the different tungsten oxide molecular structures [2–5,7,11,13,14,19]. The Raman spectra were collected with a single monochromator Horiba-Jobin Yvon LabRam HR system employing 532 nm laser excitation (Spectra Physics Model 164, Yag doubled diode pumped laser, 20 mW) and possessing a LN CCD detector (JY-CCD3000V). The catalysts were dehydrated in an *in situ* cell (Linkam T1500) by flowing 10% O_2/He at 450 °C for 1 h, and cooled to room temperature before the spectra were collected.

2.4. UV–vis-NIR diffuse reflectance spectroscopy (DRS)

The electronic structure of the supported tungsten oxide phases was determined with UV–vis diffuse reflectance spectroscopy (Varian Cary 5E UV–vis-NIR spectrophotometer). An *in situ* cell (Harrick, HVC-DR2) was employed to dehydrate the supported tungsten oxide catalysts at 400 °C in flowing 10% O_2/He for 1 h, and the UV–vis spectra were collected after cooling the sample to room temperature. A magnesium oxide reference was used for the baseline standard. The Kubelka-Munk function $F(R\infty)$ was extracted from the UV–vis DRS absorbance and the edge energy (E_g) for allowed transitions was determined by finding the intercept of the straight line in the low-energy rise of the plot of $[F(R_{oo}) \times h\nu]^2$ against $h\nu$, where $h\nu$ is the incident photon energy [45]. In order to properly determine the E_g values of the WO_3 particles present above monolayer surface coverage, the spectrum for monolayer absorbance was background subtracted to ensure that only the electronic structure of the WO_3 particles was determined.

2.5. CH_3OH temperature-programmed surface reaction (TPSR) spectroscopy

The surface acidity properties of the supported tungsten oxide catalysts were chemically probed with CH_3OH-TPSR (Altamira AMI-200) equipped with an online quadrupole mass spectrometer (Dycor Dymaxion DME200MS). In the presence of surface acid sites, methanol dehydrates to yield CH_3OCH_3 (DME) [46]. The catalysts were pretreated at 400 °C in flowing 10% O_2/He for 40 min to dehydrate the samples and remove any possible oxidizable surface residues. The catalysts were subsequently cooled in the oxidizing environment to 110 °C, then switched to flowing He and further cooled to 100 °C. The methanol was chemisorbed at 100 °C by flowing a 2000 ppm CH_3OH/He mixture for 30 min. The catalyst was initially purged for 1 h in flowing He to remove any physically adsorbed CH_3OH and then the sample temperature was increased in flowing He at a heating rate of 10 °C/min. The resulting CH_3OCH_3 ($m/e = 45$) TPSR spectra were analyzed to extract the surface kinetics of this first-order reaction that involves the rate-determining step of C–O scission of the surface methoxy intermediate [47]. The DME formation activation energy, E_a, was calculated with the first-order Redhead equation [48]:

$$\frac{E_a}{RT_P^2} = \frac{\nu}{\beta}\exp\left(-\frac{E_a}{RT_P}\right) \quad (1)$$

where T_p represents the TPSR peak temperature, $\nu = 10^{13}\ s^{-1}$ for first-order kinetics, β the heating rate (10 °C/min) and R is the gas constant. Determination of the E_a values allowed

comparison of the k_{rds} values of the different catalysts at a reference temperature.

3. Results and discussion

3.1. Molecular and electronic structures of model supported tungsten oxide catalysts

The Raman spectra of dehydrated supported WO_3/ZrO_2 catalysts are presented in Fig. 1 as a function of tungsten oxide loading (W/nm^2). The Raman band appearing in the 990–1020 cm^{-1} region is characteristic of the terminal W=O bond of the dehydrated surface WO_x species and continuously shifts from 990 to 1020 cm^{-1} with increasing tungsten oxide loading [13]. This shift of the Raman band parallels the continuous increase in the surface polytungstate/monotungstate ratio with increasing tungsten oxide loading (see UV–vis section below). This suggests that the surface monotungstate species exhibit a W=O vibration at ~990–1000 cm^{-1} and the surface polytungstate species possess its W=O vibration at ~1020 cm^{-1}, and that the shift from ~990 to 1020 cm^{-1} is related to the increasing surface polytungstate/monotungstate ratio with surface tungsten oxide coverage. The Raman bands of crystalline WO_3 NPs (805 and 715 cm^{-1}) begin to appear at ~4 W/nm^2, and continuously increase with increasing tungsten oxide loading. The appearance of crystalline WO_3 NPs generally signifies that a close packed monolayer of surface tungsten oxide has been achieved and that no additional exposed support sites remain for additional anchoring of surface WO_x species to the support [4,14]. The absence of exposed support sites is further confirmed by CH_3OH chemisorption IR experiments that demonstrate that surface support-OCH_3 sites, as well as reactive support-OH sites, are not present at monolayer coverage and that only surface W–OCH_3 sites are present at monolayer and higher surface WO_x coverage [47,49].

The surface tungsten oxide density for monolayer surface coverage can be quantified by plotting the intensity of the Raman band for the surface WO_x species and normalizing it against the ZrO_2 support Raman band at ~480 cm^{-1}, an internal standard, as a function of W/nm^2. As can be seen in Fig. 2, the normalized intensity of the surface WO_x species increases linearly with increasing tungsten oxide loading until ~4.5 W/nm^2 and remains constant at higher tungsten oxide loadings. Thus, monolayer surface coverage for surface WO_x species on the model preformed ZrO_2 support is achieved at ~4.5 W/nm^2. Similar findings were also observed for the model supported WO_3/Al_2O_3, WO_3/TiO_2 and WO_3/Nb_2O_5 catalysts. This value of monolayer surface coverage for surface WO_x species has always been reported in the catalysis literature for such model supported tungsten oxide catalysts [2,4,5,7,10,11,13,18,20,25–28,43,44].

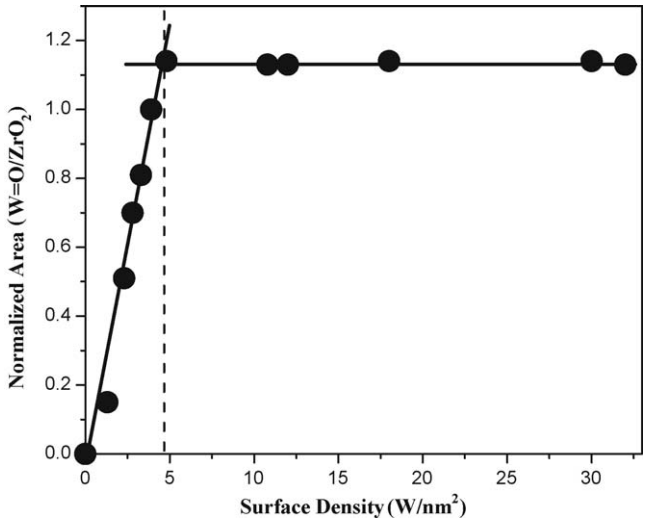

Fig. 2. Intensity of the W=O Raman band of the surface WO_x species (992–1018 cm^{-1}), normalized by the intensity of ZrO_2 support Raman band at 480 cm^{-1} as an internal standard, as a function of surface W density (W/nm^2).

The UV–vis E_g values for the dehydrated supported WO_3/ZrO_2 catalysts are presented in Fig. 3 as a function of tungsten oxide loading. The E_g values continuously decreases with increasing surface WO_x coverage. At the lowest W/nm^2 surface density, the E_g value is ~4.5 eV and is similar to the value for

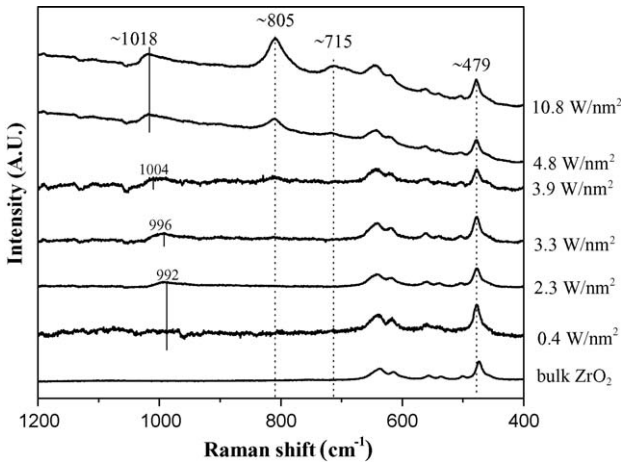

Fig. 1. Raman spectra of the dehydrated supported WO_3/ZrO_2 catalysts as a function of surface W density (W/nm^2).

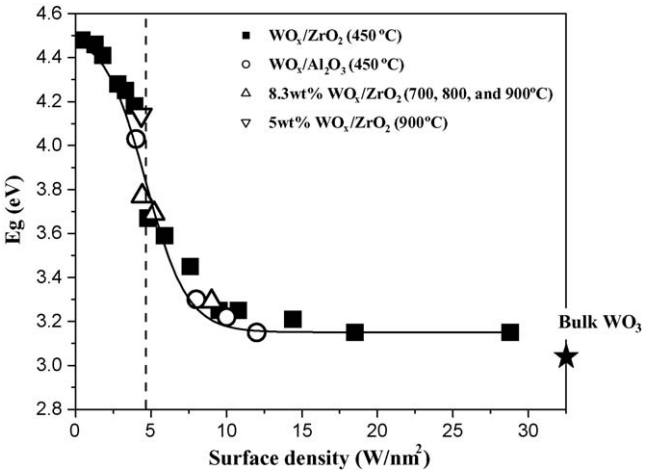

Fig. 3. Edge energy, E_g (eV), for supported WO_3 catalysts as a function of surface W density (W/nm^2). Monolayer surface coverage, 4.5 W/nm^2, is represented by the vertical dashed line.

reference compounds possessing isolated WO_4 or WO_6 structures (e.g., Na_2WO_4, $NiWO_4$, respectively) [47]. At a surface density of 4.5 W/nm^2, monolayer surface coverage, an E_g value of ~4.2 eV is obtained and corresponds to the value found for reference compounds consisting of polymeric WO_x chains (e.g., $Na_2W_2O_7$, which consists of alternating WO_4 and WO_6 units) [47]. Above 4.5 W/nm^2, the E_g values continue to decrease with increasing tungsten oxide loading until about 9 W/nm^2. This continuous decrease from 4.5 to 9 W/nm^2 is related to the presence of the crystalline WO_3 NPs present above monolayer surface coverage, which is consistent with the Raman results presented above. The E_g values for the WO_3 NPs, however, are higher than that for bulk WO_3 (E_g = 2.8 eV) because of the quantum confinement effect of these small nanoparticles. Above 9 W/nm^2, the E_g value is relatively constant and close to the value for large bulk WO_3 particles that are present at such high surface WO_x density. The surface WO_x density on ZrO_2 could also be varied by raising the calcination temperature, which resulted in sintering the ZrO_2 support and, consequently, increasing the surface W density. The E_g values for such a series of supported WO_3/ZrO_2 catalysts calcined at elevated temperatures are also plotted in Fig. 3 and also fall on the same curve as a function of surface W density. Furthermore, the E_g values for supported WO_3/Al_2O_3 catalysts as a function of tungsten oxide loading are also shown in Fig. 3 and their values exactly overlay those of the supported WO_3/ZrO_2 catalyst system as a function of W/nm^2. The strong UV–vis absorption by the TiO_2 and Nb_2O_5 supports prevents the accurate determination of the E_g values for the supported tungsten oxide phases on these supports. Thus, the E_g value only depends on the surface W density and is related to the molecular structure of the supported tungsten oxide phase.

In summary, the surface tungsten oxide phases on the examined supports consists of (i) isolated surface monotungstate and polytungstate species below monolayer surface coverage (<4.5 W/nm^2) with increasing poly/mono ratio with loading in this region, (ii) crystalline WO_3 NPs (4.5 < W < 9 W/nm^2), and large, bulk-like WO_3 particles (>9 W/nm^2). Previous XANES structural studies revealed that the dehydrated surface WO_x species on model supports at low surface coverage tend to be present in WO_4 coordination at low surface coverage and WO_5/WO_6 coordination at high surface coverage [7,10]. Comparison with the current UV–vis and Raman data reveals that the isolated surface monotungstate species possess WO_4 coordination and the surface polytungstate species possess WO_5/WO_6 coordination. Furthermore, the Raman shift from ~990 to 1020 cm^{-1} with surface WO_x coverage suggests that the surface monotungstate WO_4 species are probably dioxo (O=W=O) structures and that the surface polytunsgtate WO_5/WO_6 species are probably monoxo (W=O) structures because dioxo functionalities generally vibrate ~20–30 cm^{-1} lower than monoxo functionalities [50].

3.2. Surface reactivity of model supported tungsten oxide catalysts

The surface acidic properties of the supported tungsten oxide phase were chemically probed with CH_3OH dehydration to CH_3OCH_3 (DME) since this reaction is known to readily proceed over surface acidic sites [46]. The methanol dehydration reaction, unfortunately, does not discriminate between surface Lewis and Broensted acid sites, which require the use of basic chemical probe molecules. Nevertheless, the methanol dehydration reaction provides fundamental information about the number of catalytic active sites and their relative acidic activity. Recent studies have revealed that this catalytic reaction proceeds via first-order kinetics where the rate-determining step is breaking of the C–O bond of the surface CH_3O^* intermediate [47]. All the supported tungsten oxide catalysts were found to almost exclusively yield DME as the reaction product, which reflects the acidic nature of the supported tungsten oxide phase.

The CH_3OH-TPSR experiments demonstrated that bulk WO_3 (T_p,W = 254 °C) has significantly more catalytic active surface acid sites than found on the pure oxide supports (T_p, Zr = 374 °C, T_p,Ti = 325 °C, T_p,Nb = 300 °C) with the exception of Al_2O_3 (T_p,Al = 196 °C). The surface tungsten oxide phase on all the supports, with the exception of Al_2O_3, introduced much more active surface acid sites to the catalysts with resulting significantly lower T_p values. In the case of surface WO_x on Al_2O_3, monolayer surface WO_x coverage resulted in the complete suppression of the very active DME T_p peak at 196 °C from the alumina support sites and the appearance of a less active DME T_p peak at ~219–226 °C from the surface WO_x species. The CH_3OH-TPSR chemical probe findings are in agreement with the CH_3OH-IR findings that no exposed surface Al_2O_3 sites are present above monolayer surface coverage for the supported WO_3/Al_2O_3 catalyst system. This is consistent with the concept of a closed packed monolayer of surface WO_x species that do not expose any support cations [51,52]. Consequently, the catalytic acid sites being probed by CH_3OH-TPSR above monolayer surface coverage are exclusively associated with the supported tungsten oxide phase and not with exposed support surface sites.

The CH_3OH-TPSR chemical reactivity results for the supported WO_3/ZrO_2 catalysts are presented in Fig. 4 as a

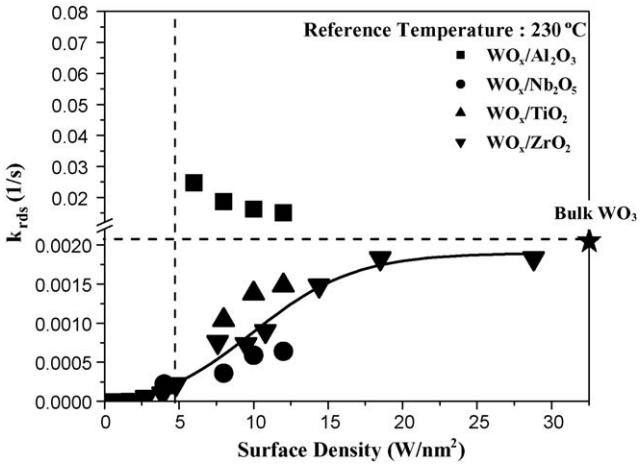

Fig. 4. First-order kinetic rate constants for CH_3OH dehydration over bulk WO_3 and supported WO_3 catalysts as a function of the surface W density (W/nm^2). Monolayer surface coverage, 4.5 W/nm^2, is represented by the vertical dashed line.

function of tungsten oxide loading where the T_p values have been converted to first-order k_{rds} values employing the Redhead equation. Although exposed surface Zr sites are present below monolayer surface coverage, they do not contribute to the kinetic results because the surface WO_x species are significantly more active than the exposed ZrO_2 sites for DME production (T_p, Zr = 374 °C and T_p, W = 254 °C). The CH_3OH-TPSR chemical probe experiments reveal that the acidic catalytic activity of the supported WO_3 catalysts increases with increasing surface tungsten oxide density, and asymptotically approaches that of bulk WO_3 above 9 W/nm^2. The same exact trends and asymptotic values were also obtained for the supported WO_3/TiO_2 and WO_3/Nb_2O_5 catalysts. An inverse trend, however, was found for the supported WO_3/Al_2O_3 catalysts with the k_{rds} monotonically decreasing with increasing surface coverage above monolayer (>4.5 W/nm^2) and asymptotically approaching that of bulk WO_3 above 9 W/nm^2 (see Fig. 4). The supported WO_3/Al_2O_3 catalyst system was not investigated below monolayer coverage because active exposed Al_2O_3 surface sites would overshadow the catalytic activity of the surface WO_x species on Al_2O_3. Furthermore, even at extremely high surface coverage of 12 W/nm^2, where exposed support sites are not present, the catalytic active sites present for WO_3/Al_2O_3 are an order of magnitude more active than found for the other supported WO_3 catalysts.

The CH_3OH-TPSR spectra also allowed for determination of the number of exposed surface WO_x sites, N_s, in the catalysts since the areas under their curves directly reflected this value. The supported WO_3 catalysts' N_s values were normalized to those obtained for ~4.5 W/nm^2 for each support since these catalysts possessed 100% dispersed surface tungsten oxide and their N_s values are quantitatively known. The N_s values are shown in Fig. 5 for supported WO_3/ZrO_2 and linearly increase from 0 to 4.5 W/nm^2 (by definition since the WO_x is 100% dispersed until monolayer), gently decrease in the 4.5–9 W/nm^2 range, and rapidly decrease above 9 W/nm^2. Similar N_s trends with W/nm^2 surface density were also observed with the other supported WO_3 catalysts above monolayer surface coverage.

Steady-state methanol dehydration catalytic studies to DME were also undertaken and the TOF values for the different catalysts are presented in Fig. 6 as a function of tungsten oxide loading and specific oxide support. The reaction rates were converted to TOF values by employing the N_s values determined from the CH_3OH-TPSR investigation. The TOF values for the supported WO_3/ZrO_2, WO_3/TiO_2 and WO_3/Nb_2O_5 catalysts increase with increasing surface tungsten oxide density up to ~9 W/nm^2 and then leveled off. For the supported WO_3/Al_2O_3 catalyst system, an inverse trend was found where the TOF value slightly decreases with increasing surface tungsten oxide density up to ~9 W/nm^2 and then levels off with increasing surface W density.

3.3. Molecular/electronic structure–acidity relationships

The molecular structures of the supported tungsten oxide phases were shown to be identical for the catalyst systems investigated: isolated surface monotungstate dioxo WO_4 species at low surface coverage (≪4.5 W/nm^2), polymeric surface polytungstate monoxo WO_5/WO_6 species also present at higher surface coverage (<4.5 W/nm^2), with the polytungstate being the dominant surface WO_x species at monolayer and higher surface coverage, WO_3 NPs between 4.5 and 9 W/nm^2, and large bulk-like WO_3 particles above 9 W/nm^2. It should be noted that the WO_3 crystallites were usually present above monolayer surface coverage and were formed on top of the surface WO_x monolayer. Furthermore, exposed support surface sites are not present for monolayer and higher surface WO_x coverage because the reactive support-OH sites are consumed by the surface WO_x species and support-OCH_3 species are not detected at monolayer surface WO_x coverage (~4.5 W/nm^2).

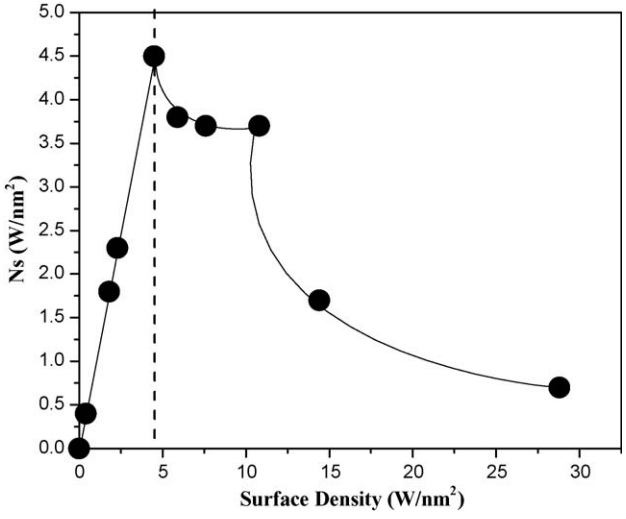

Fig. 5. Number of exposed W sites/nm^2 for supported WO_3/ZrO_2 catalysts as a function of surface W density (W/nm^2). Monolayer surface coverage, 4.5 W/nm^2, is represented by the vertical dashed line.

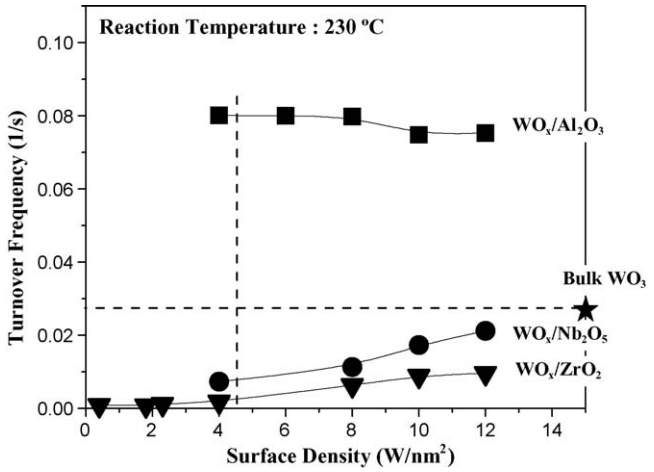

Fig. 6. CH_3OH dehydration TOF values for different supported WO_3 catalyst systems as well as the TOF for bulk WO_3 as a function of surface W density (W/nm^2). Monolayer surface coverage, 4.5 W/nm^2, is represented by a vertical dashed line.

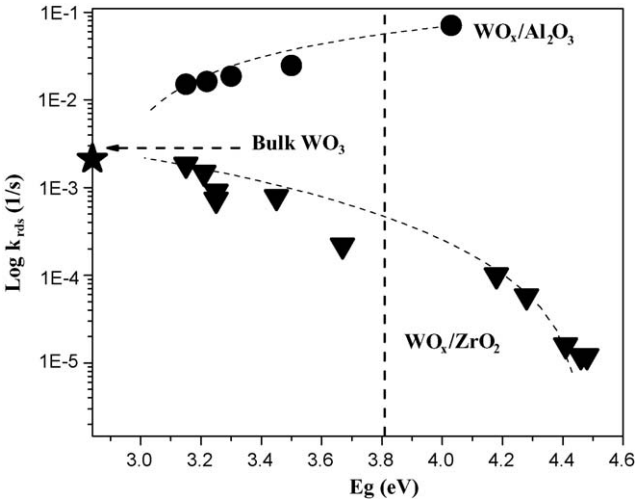

Fig. 7. Log of the first-order kinetic rate constant for CH_3OH dehydration, k_{rds}, as a function of edge energy, E_g. Monolayer surface coverage, 4.5 W/nm^2, is represented by a vertical dashed line.

The corresponding electronic structures of the different tungsten oxide structures reflect their domain size: monotungstate < polytungstate < WO_3 NP < bulk-like WO_3 particle. The E_g value reflects the degree of electron delocalization in the tungsten oxide phase and decreases with increasing tungsten oxide domain size. Consequently, larger tungsten oxide domains allows for greater electron delocalization. The methanol dehydration first-order k_{rds} reaction rate constant is plotted versus E_g for the supported WO_3/ZrO_2 and WO_3/Al_2O_3 catalysts in Fig. 7. As mentioned earlier, the E_g values for the supported WO_3/TiO_2 and WO_3/Nb_2O_5 catalyst systems could not be determined because of the strong UV–vis absorption by these oxide supports. For the supported WO_3/ZrO_2 catalyst system, the k_{rds} reaction rate constant increases with surface tungsten oxide density while the electronic E_g values decrease. The opposite is trend is observed for the k_{rds} reaction rate for supported WO_3/Al_2O_3. The curves in Fig. 7 demonstrate that no unique relationship can be established between the methanol dehydration k_{rds} and the electronic structure of the different tungsten oxide domains because of the complete opposite variations of the two curves. Similar trends are also obtained when TOF is plotted versus E_g. Thus, another explanation must be responsible for these trends.

The one structural parameter that is uniquely different for all the investigated supported WO_3 catalysts is the different oxide supports. The surface WO_x species on Al_2O_3 are significantly more active than the surface WO_x species on the oxide supports. The high electronegativity of the Al ligand results in a less basic or more acidic bridging W–O–Al bond [53]. The lower electronegativity of the other support cations, makes the bridging W–O–M bonds more basic or less acidic. The enhanced catalytic acidity of the surface WO_x species on Al_2O_3 results in this tungsten oxide structure being more active than the WO_3 NPs and bulk-like WO_3 particles. The relatively low catalytic acidity of the surface WO_x species on ZrO_2, TiO_2 and Nb_2O_5 makes this tungsten oxide structure somewhat less active than the WO_3 NPs and bulk-like WO_3 particles. Thus, it is the relative catalytic acidity of the surface WO_x species, which is controlled by the specific support, that determines the activity trend as a function of surface W density in going from surface WO_x to WO_3 NPs to bulk-like WO_3 particles.

4. Conclusion

A series of supported WO_3 catalysts were synthesized on Al_2O_3, Nb_2O_5, TiO_2 and ZrO_2 supports as a function of tungsten oxide loading. The molecular structure and monolayer surface coverage of the supported tungsten oxide phase was determined with UV–vis and Raman spectroscopy, respectively. The same tungsten oxide species were found to be present on all the supports as a function of surface tungsten oxide density (W/nm^2) with monolayer surface coverage corresponding to 4.5 W/nm^2: surface monotungstate WO_4 species ($\ll$4.5 W/nm^2), surface polytungstate WO_5/WO_6 species (<4.5 W/nm^2), WO_3 NPs (4.5–9 W/nm^2), and large bulk-like WO_3 particles (>9 W/nm^2). The edge energy (E_g) of all the supported tungsten oxide catalysts monotonically decreased with increasing tungsten oxide domain size (W/nm^2) indicating greater electron delocalization. The specific solid acidity of the supported tungsten oxide catalysts, however, was not found to correlate with either the tungsten oxide molecular structures or electronic structures. This was a consequence of the acidic catalytic activity of the surface monotungstate and polytungstate species relative to the WO_3 NPs and the bulk-like WO_3 particles. For the supported WO_3/Al_2O_3 catalyst system, the surface WO_x species are more active than the crystalline WO_3 particles and, consequently, the overall specific acidic catalytic activity (TOF) decreases with increasing surface W/nm^2 density as WO_3 NPs are introduced. For the other supported WO_3 catalyst systems (WO_3/Nb_2O_5, WO_3/TiO_2 and WO_3/ZrO_2), the surface WO_x species are less active than the crystalline WO_3 particles and, consequently, the overall specific acidic catalytic activity (TOF) increases with increasing surface W/nm^2 density as WO_3 NPs are introduced. Consequently, no universal molecular/electronic structure–solid acidity relationships exist for supported WO_3 catalysts.

Acknowledgement

This research was performed with the financial assistance of a DOE-Basic Energy Sciences grant (DOE-FG02-93ER14350).

References

[1] R. Thomas, F.P.J.M. Kerkhof, J.A. Moulijn, J. Medema, V.H.J. de Beer, J. Catal. 61 (1980) 559.
[2] L. Salvati, L.E. Makovsky, J.M. Stencel, F.R. Brown, D.M. Hercules, J. Phys. Chem. 85 (1981) 3700.
[3] S.S. Chan, I.E. Wachs, L.L. Murrell, L. Wang, W.K. Hall, J. Phys. Chem. 88 (1984) 5831.
[4] S.S. Chan, I.E. Wachs, L.L. Murrell, N.C. Dispenziere, J. Catal. 92 (1985) 1.
[5] S.L. Soled, L.L. Murrell, I.E. Wachs, G.B McVicker, L.G. Sherman, S.S. Chan, N.C. Dispenziere, R.T. Baker, Solid State Chem. Catal: ACS Symp. Ser. 275 (1985) 161.

[6] J. Bernholc, J.A. Horsley, L.L. Murrell, L.G. Sherman, S.L. Soled, J. Phys. Chem. 91 (1987) 1526.
[7] J.A. Horsley, I.E. Wachs, J.M. Brown, G.H. Via, F.D. Hardcastle, J. Phys. Chem. 91 (1987) 4014.
[8] M. Hino, K. Arata, J. Chem. Soc. Chem. Commun. 18 (1988) 1259.
[9] M. Hino, K. Arata, Chem. Lett. 6 (1989) 971.
[10] F. Hilbrig, H.E. Goebel, H. Knoezinger, H. Schmelz, B. Lengeler, J. Phys. Chem. 95 (1991) 6973.
[11] M.A. Vuurman, I.E. Wachs, J. Phys. Chem. 96 (1992) 5008.
[12] A.M. Turek, E. DeCanio, I.E. Wachs, J. Phys. Chem. 96 (1992) 5000.
[13] D.S. Kim, M. Ostromecki, I.E. Wachs, J. Mol. Catal A: Chem. 106 (1996) 93.
[14] I.E. Wachs, Catal. Today 27 (1996) 437.
[15] R.A. Boyse, E.I. Ko, J. Catal. 171 (1997) 191.
[16] J.G. Santiesteban, J.C. Vartuli, S. Han, R.D. Bastian, C.D. Chang, J. Catal. 168 (1997) 431.
[17] M. Scheithauer, R.K. Grasselli, H. Knozinger, Langmuir 14 (1998) 3019.
[18] N. Vaidyanathan, M. Houalla, D.M. Hercules, Surf. Interface Anal. 26 (1998) 415.
[19] M. Scheithauer, T.K. Cheung, R.E. Jentoft, R.K. Grasselli, B.C. Gates, H. Knozinger, J. Catal. 180 (1998) 1.
[20] N. Naito, N. Katada, M. Niwa, J. Phys. Chem. B 103 (1999) 7206.
[21] D.G. Barton, M. Shtein, R.D. Wilson, S.L. Soled, E. Iglesia, J. Phys. Chem. B 103 (1999) 630.
[22] S. Eibl, B.C. Gates, H. Knozinger, Langmuir 17 (2001) 107.
[23] C.D. Baertsch, S.L. Soled, E. Iglesia, J. Phys. Chem. B 105 (2001) 1320.
[24] C.D. Baertsch, K.T. Komala, Y.H. Chua, E. Iglesia, J. Catal. 205 (2002) 44.
[25] M. Valigi, D. Gazzoli, I. Pettiti, G. Mattei, S. Colonna, S. DeRossi, G. Ferraris, Appl. Catal.A: Gen. 231 (2002) 159.
[26] N. Vaidyanathan, D.M. Hercules, M. Houalla, Anal. Bioanal. Chem. 373 (2002) 547.
[27] G. Ferraris, S. De Rossi, D. Gazzoli, I. Pettiti, M. Valigi, G. Magnacca, C. Morterra, Appl. Catal. A: Gen. 240 (2003) 119.
[28] M. Niwa, Y. Habuta, K. Okumura, N. Katada, Catal. Today 87 (2003) 213.
[29] J. Macht, C.D. Baertsch, M.M. Lozano, S.L. Soled, Y. Wang, E. Iglesia, J. Catal. 227 (2004) 479.
[30] S. Sarish, B.M. Devassy, S.B. Halligudi, J. Mol. Catal. A: Chem. 235 (2005) 44.
[31] C.L. Thomas, Catalytic Processes and Proven Catalysts, Academic Press, New York, 1970.
[32] C.N. Satterfield, Heterogeneous Catalysis in Practice, McGraw-Hill, New York, 1980.
[33] L.L. Murrell, C.J. Kim, D.C. Grenoble, U.S. Patent No. 4,233,139 (1980).
[34] C. Wivel, B.S. Clausen, R. Candia, S. Morup, H. Topsoe, J. Catal. 87 (1984) 497.
[35] D.C. Grenoble, C.J. Kim, L.L. Murrell, U.S. Patent No. 4,440,872 (1984).
[36] L.L. Murrell, D.C. Grenoble, C.J. Kim, N.C. Dispenziere, J. Catal. 107 (1987) 463.
[37] J.P. Chen, R.T. Yang, Appl. Catal. A: Gen. 80 (1992) 135.
[38] D. Djerad, L. Tifouti, M. Crocoll, W. Weisweiler, J. Mol. Catal. A: Chem. 208 (2004) 257.
[39] G. Baltin, H. Koser, K.P. Wendlandt, Catal. Today 75 (2002) 339.
[40] M. Ai, J. Catal. 49 (1977) 305.
[41] S. Morikawa, K. Takahashi, J. Mogi, S. Kurita, Bull. Chem. Soc. Jpn. 55 (1982) 2254.
[42] F. Verpoort, A.R. Bossuyt, L. Verdonck, J. Mol. Catal. A: Chem. 95 (1995) 75.
[43] L. Lietti, J.L. Alemany, P. Forzatti, G. Busca, G. Ramis, E. Giamello, F. Bregani, Catal. Today 29 (1996) 143.
[44] C. Martín, G. Solana, P. Malet, V. Rives, Catal. Today 78 (2003) 365.
[45] W.N. Delgass, G.L. Haller, R. Kellerman, J.H. Lunsford, Spectroscopy in Heterogeneous Catalysts, Academic Press, New York, 1979.
[46] J.M. Tatibouet, J. Appl. Catal. A: Gen. 148 (1997) 205.
[47] E.I. Ross, T. Kim, W.V. Knolls, M.S. Wong, I.E. Wachs, in press.
[48] P.A. Redhead, Vacuum 12 (1962) 213.
[49] L.J. Burcham, L.E. Briand, I.E. Wachs, Langmuir 17 (2001) 6164.
[50] K. Nakamoto, Infrared and Raman Spectra of Inorganic and coordination Compounds, 5th ed., Wiley, New York, 1997.
[51] L.E. Briand, O.P. Tkachenko, M. Guraya, X. Gao, I.E. Wachs, W. Griinert, J. Phys. Chem. B 108 (2004) 4823.
[52] L.E. Briand, O.P. Tkachenko, M. Guraya, I.E. Wachs, W. Gruenert, Surf. Interface Anal. 36 (2004) 238.
[53] I.E. Wachs, Catal. Today 100 (2005) 79.